Supplementary Information (SI) for New Journal of Chemistry.
This journal is © The Royal Society of Chemistry and the Centre National de la Recherche Scientifique 2026

Supporting Information

In Situ Grown $CuSiO_X$ Nanoflowers on Carbon Nanofibers for Electrochemical CO_2 Reduction to Methane

Fangfang Zhong, Penggao Liu, Xueyan Wu, Xingyun Li, Yan Lv, Jixi Guo**

State Key Laboratory of Chemistry and Utilization of Carbon Based Energy Resources;

College of Chemistry, Xinjiang University, Urumqi, 830017, Xinjiang, P.R. China.

E-mail: lvyan2014@xju.edu.cn; jxguo1012@163.com; jdz@xju.edu.cn

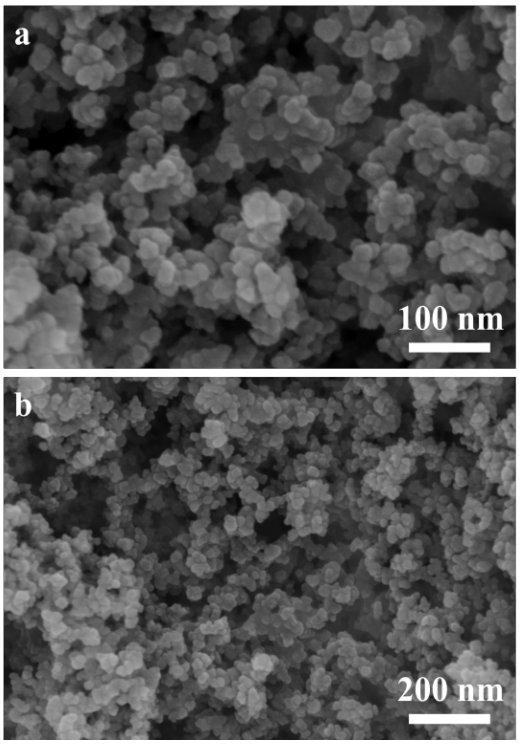

Fig. S1 (a, b) SEM images of SiO_2.

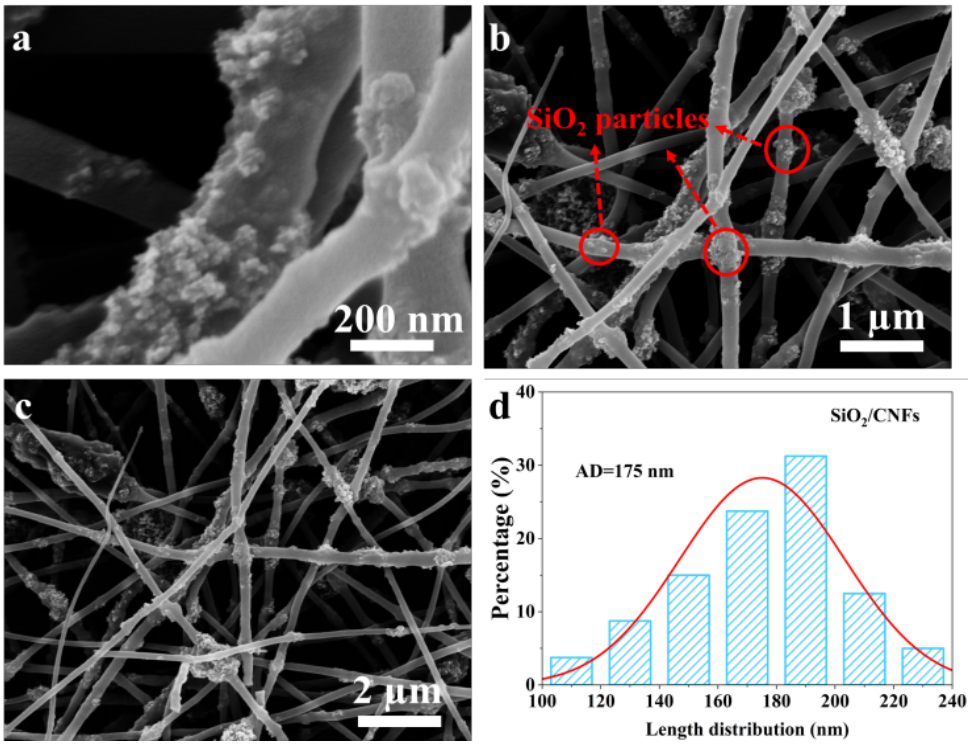

Fig. S2 SEM images of (a-c) SiO_2/CNFs, and (d) diameter size distribution of SiO_2/CNFs.

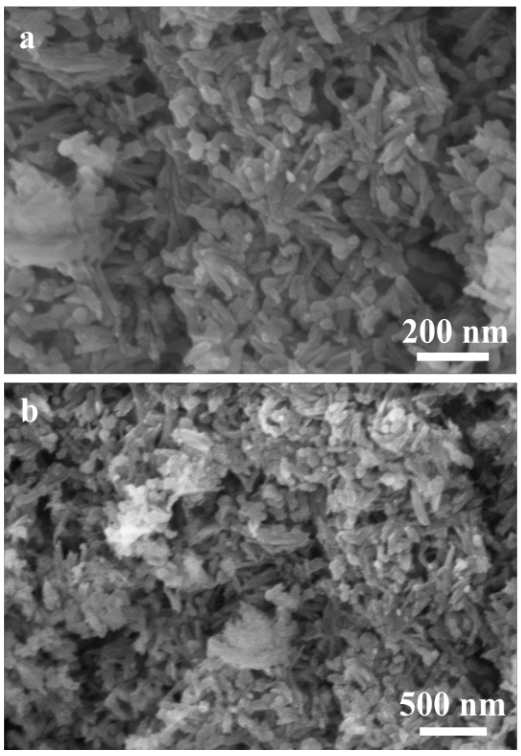

Fig. S3 (a, b) SEM images of $CuSiO_3$.

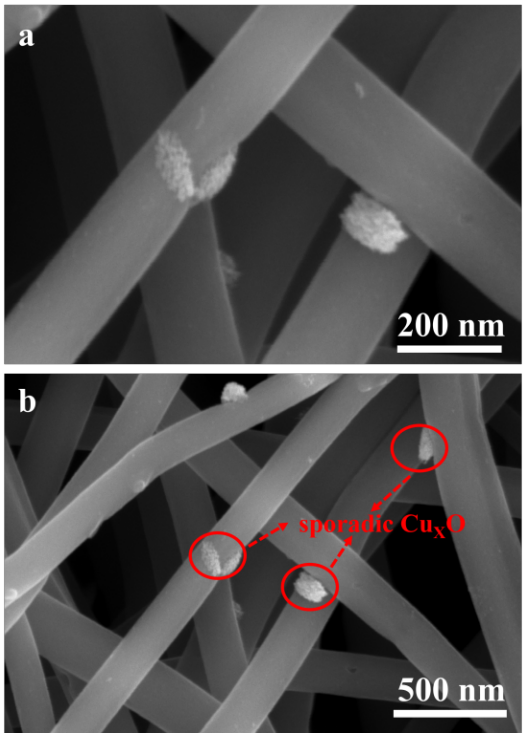

Fig. S4 (a, b) SEM images of Cu_XO/CNFs.

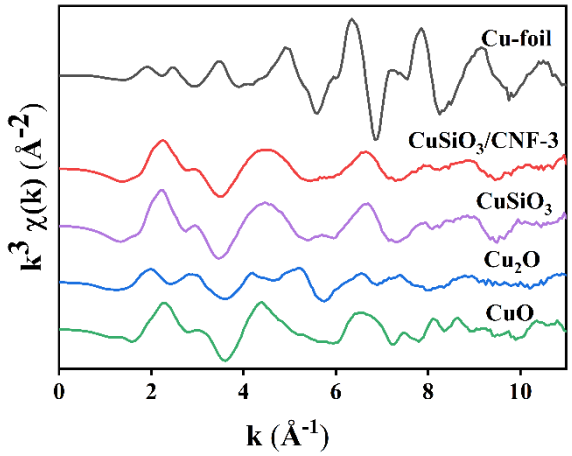

Fig. S5 Cu k-edge EXAFS for Cu foil, CuO, Cu_2O, $CuSiO_3$/CNFs-3 and $CuSiO_3$.

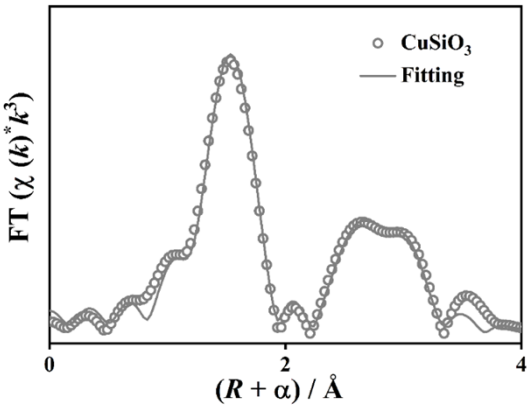

Fig. S6 The corresponding EXAFS fitting curve for $CuSiO_3$.

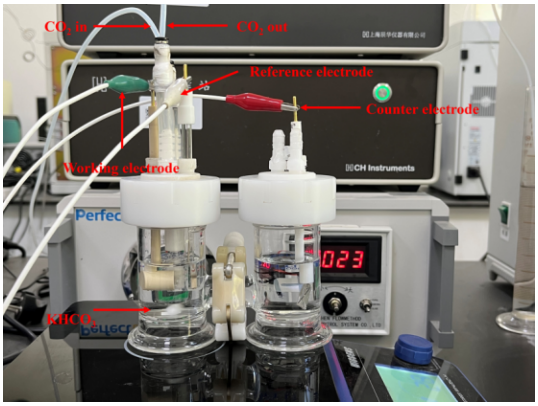

Fig. S7 Diagram of three-electrode air-tight H-type electrolytic cell.

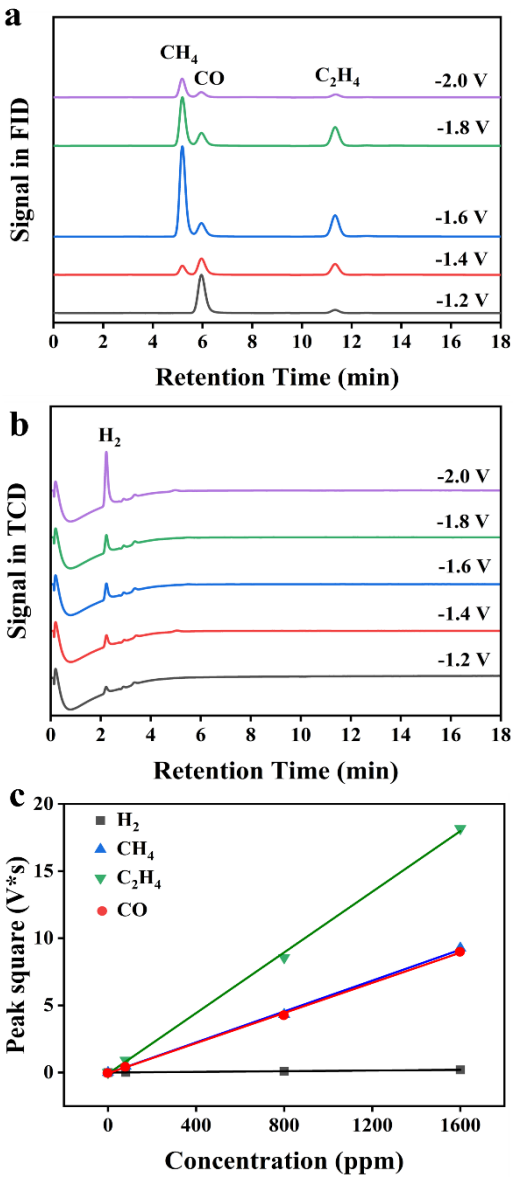

Fig. S8 In-stiu-gas-chromatography spectra under various potentials of $CuSiO_3$/CNFs-3 in chronoamperometry detected by (a) FID; (b) TCD detectors and (c) Standard curve.

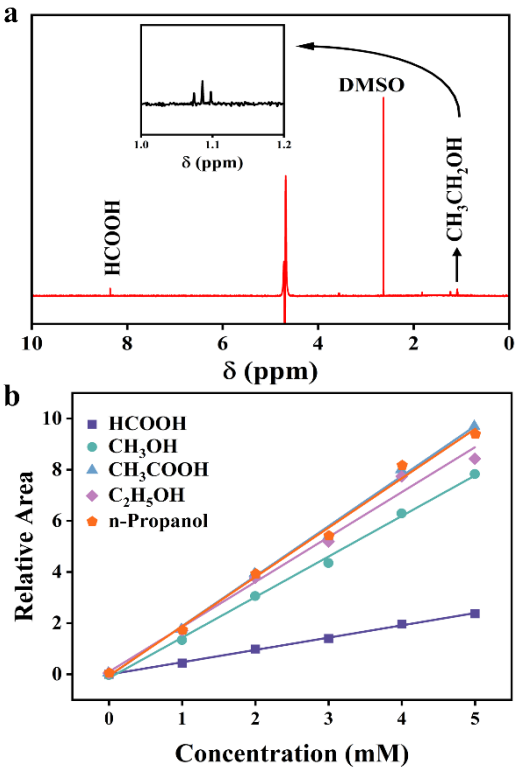

Fig. S9 (a) ^{1}H NMR spectra of the electrolyte for CO_2RR at −1.6 V (vs. RHE) using $CuSiO_3$/CNFs-3; (b) Standard curve. DMSO is used as an internal standard.

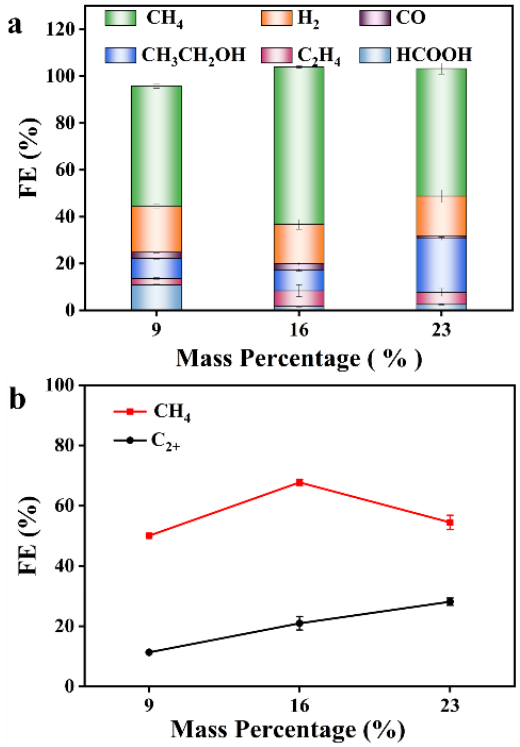

Fig. S10 FEs of CO_2RR products on catalyst at different the mass of SiO_2: (a) gas and liquid products; (b) CH_4 and C_{2+}.

At −1.6 V (vs. RHE), as the silica content increases, FE_{CH4} follows a volcano-shaped trend, while the FE_{C2+} reduction products significantly increases from 11.3% to 28.2%.

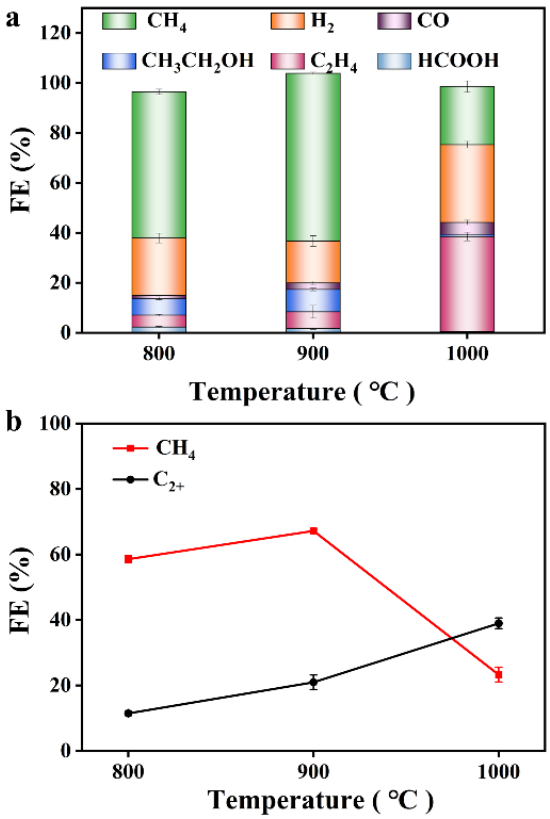

Fig. S11 FEs of CO_2RR products on catalyst at different the carbonization temperature: (a) gas and liquid products; (b) CH_4 and C_{2+}.

At −1.6 V (vs. RHE), as the carbonization temperature increases from 800 °C to 1000 °C, the FE_{CH4} exhibits a volcano-shaped trend, while the Faradaic efficiency for CO_2 reduction (FE_{C2+}) products significantly increases from 11.4% to 38.4%.

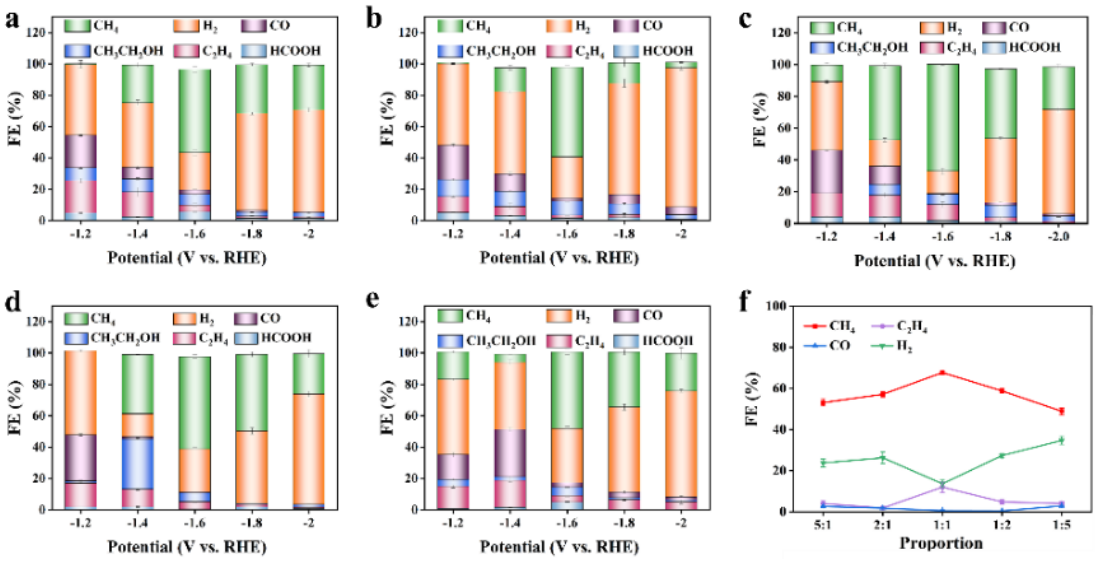

Fig. S12 FEs of CO_2RR products on catalyst at different the mass ratio of SiO_2/CNFs to copper salts: (a) 5:1; (b) 2:1; (c) 1:1; (d) 1:2; (e) 1:5; (f) gas products.

At −1.6 V (vs. RHE), when adjusting the ratio of SiO_2/CNFs to Cu salts, we found that the main product of the catalyst is CH_4, with the Faradaic efficiency (FE) for CH_4 consistently around 50%, and the 1:1 ratio is the optimal.

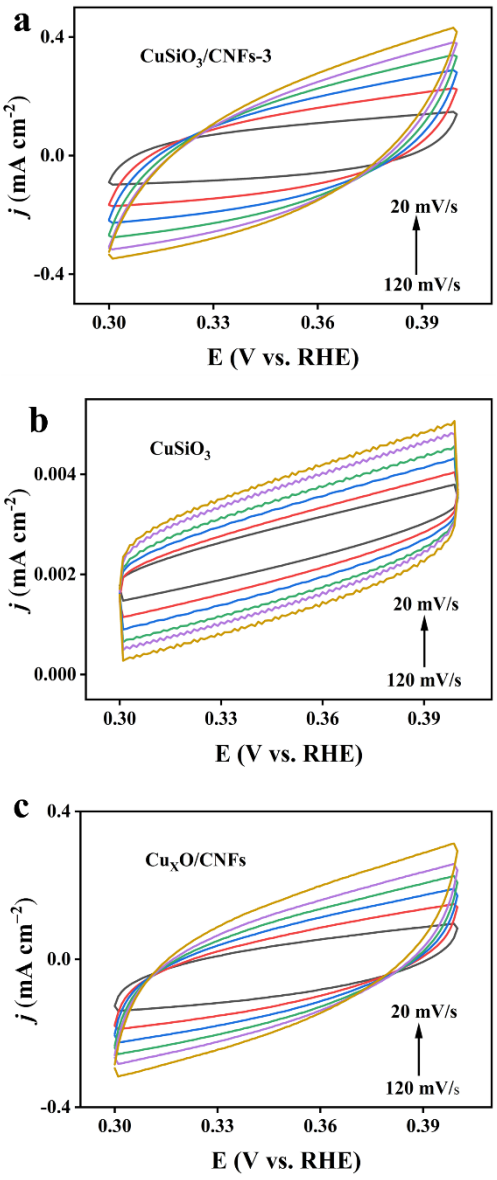

Fig. S13 CV curves of (a) $CuSiO_3$/CNFs-3, (b) $CuSiO_3$, (c) Cu_XO/CNFs.

Electrochemically active surface area (ECSA): $ECSA = R_f \times S$

S is the real surface area, which was generally equal to the geometric area of glassy carbon electrode (S = 0.2827433 cm^{-2}). The roughness factor R_f is estimated from the ratio of double-layer capacitance C_{dl} for the working electrode (assuming that the average double-layer capacitance of a smooth metal surface is 20 μF cm^{-2})[1], that is, $R_f = C_{dl}/20$ μF cm^{-2}.

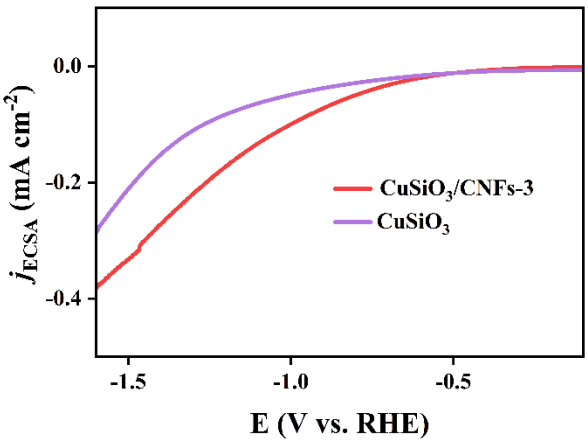

Fig. S14 Normalized LSV curves of $CuSiO_3$/CNFs-3 and $CuSiO_3$ to the electrochemically active surface area.

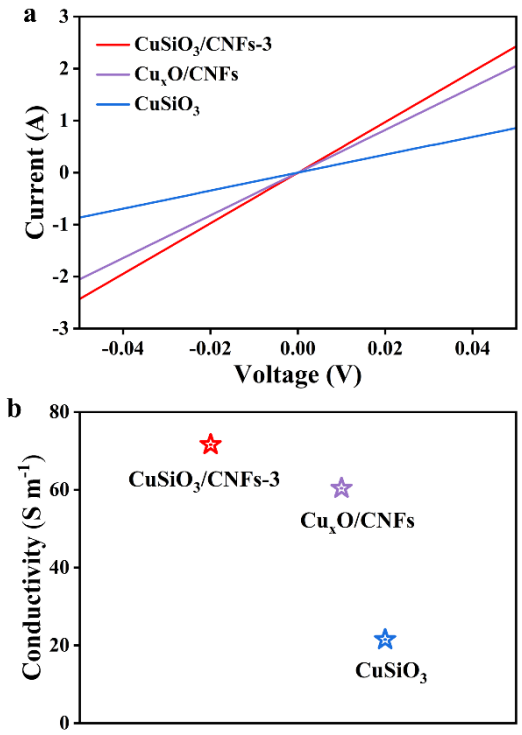

Fig. S15 I−V curves of (a) $CuSiO_3$/CNFs-3、$CuSiO_3$、Cu_XO/CNFs and (b) conductivity.

The conductance is calculated as follows:

$$\rho = R \times S / I$$

$$\delta = 1/\rho$$

Where R is the resistance, I indicate the thickness of the piece being measured and S is the contact area.

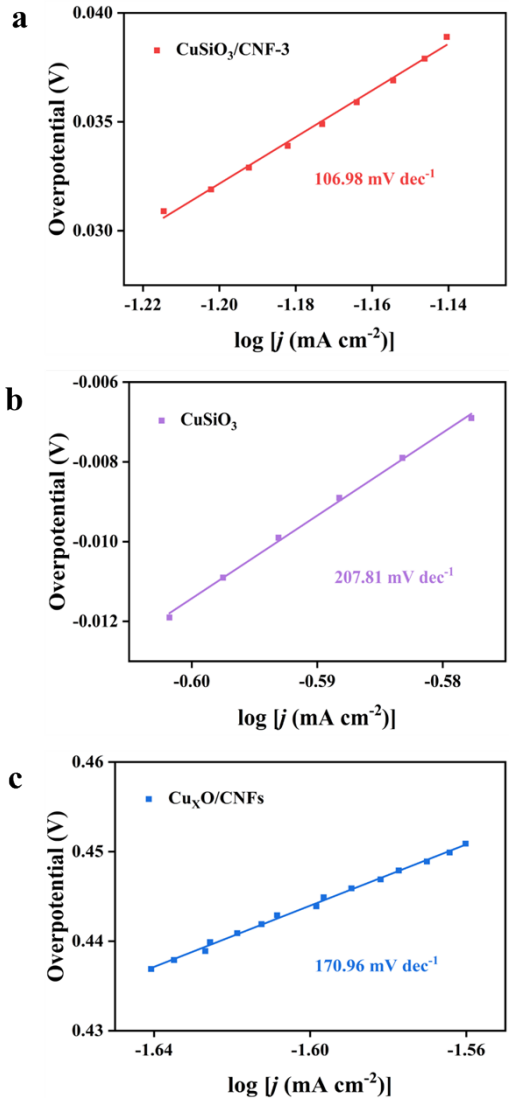

Fig. S16 Tafel slopes of $CuSiO_3$/CNFs-3、$CuSiO_3$、Cu_XO/CNFs.

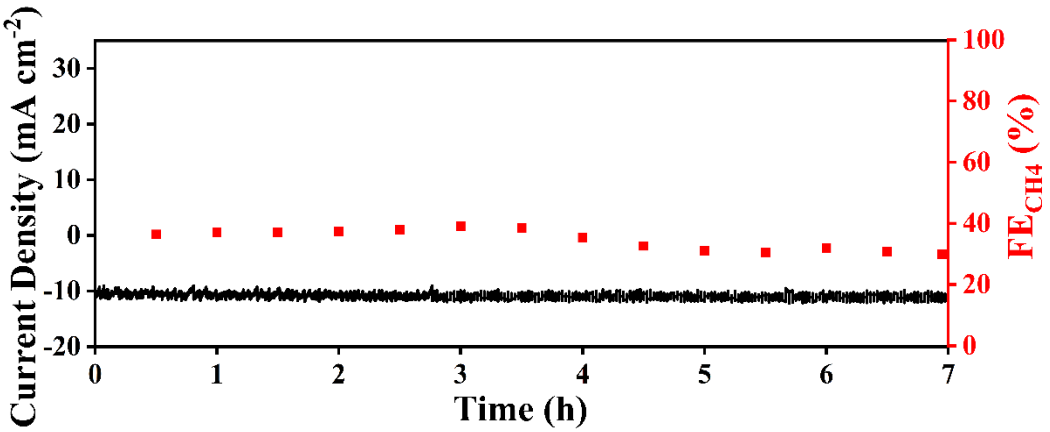

Fig. S17 Stability test of $CuSiO_3$ at the highest CO_2RR Faradaic efficiency potential.

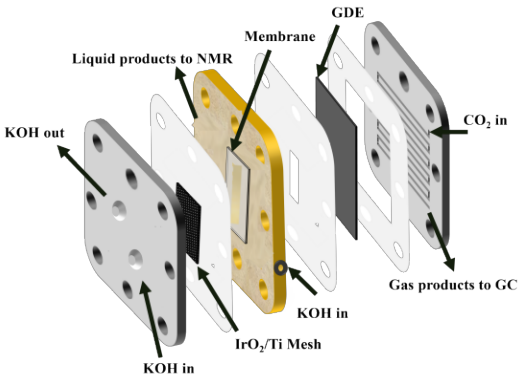

Fig. S18 Diagram of flow cell device.

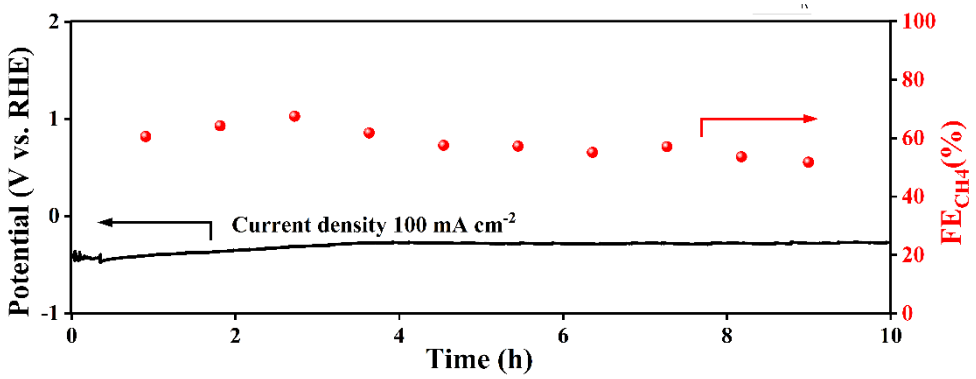

Fig. S19 Stability of $CuSiO_3$/CNFs-3 at 100 mA cm^{-2} in flow cell.

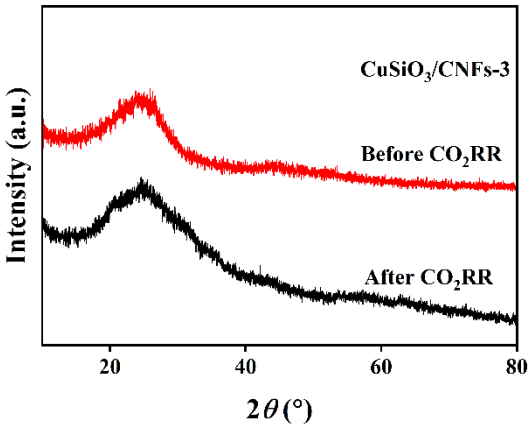

Fig. S20 XRD patterns of (a, b) $CuSiO_3$/CNFs-3 after CO_2RR reaction.

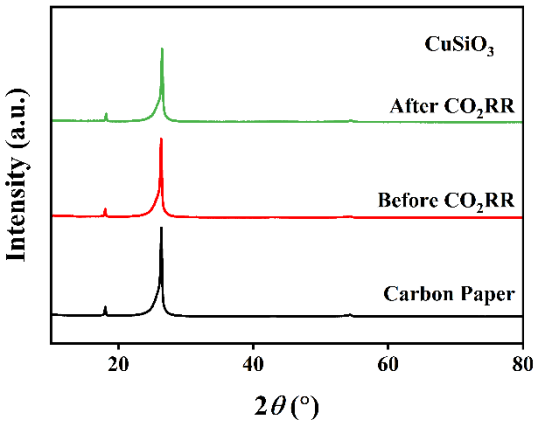

Fig. S21 XRD patterns of $CuSiO_3$ after CO_2RR reaction.

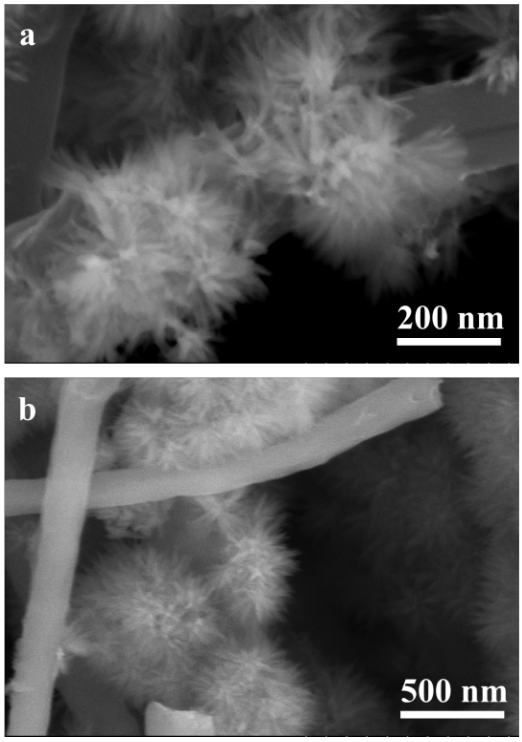

Fig. S22 (a, b) SEM images of the $CuSiO_3$/CNFs-3 sample after electroreduction.

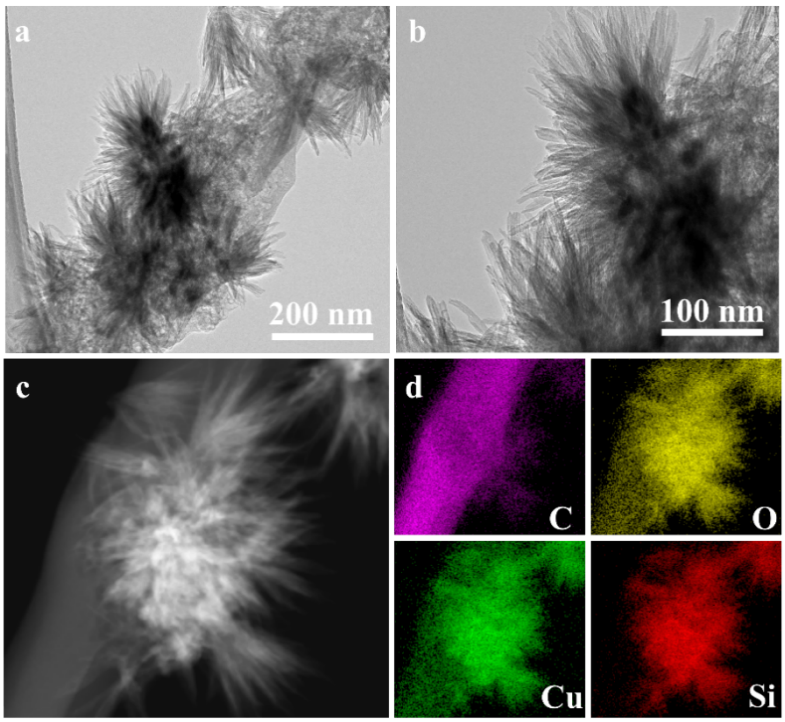

Fig. S23 (a-d) TEM images of the $CuSiO_3$/CNFs-3 after electroreduction.

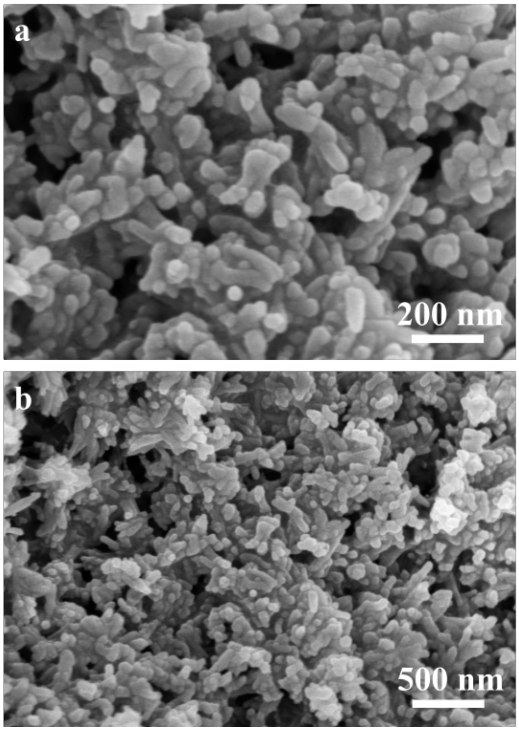

Fig. S24 (a, b) SEM images of the $CuSiO_3$ sample after electroreduction.

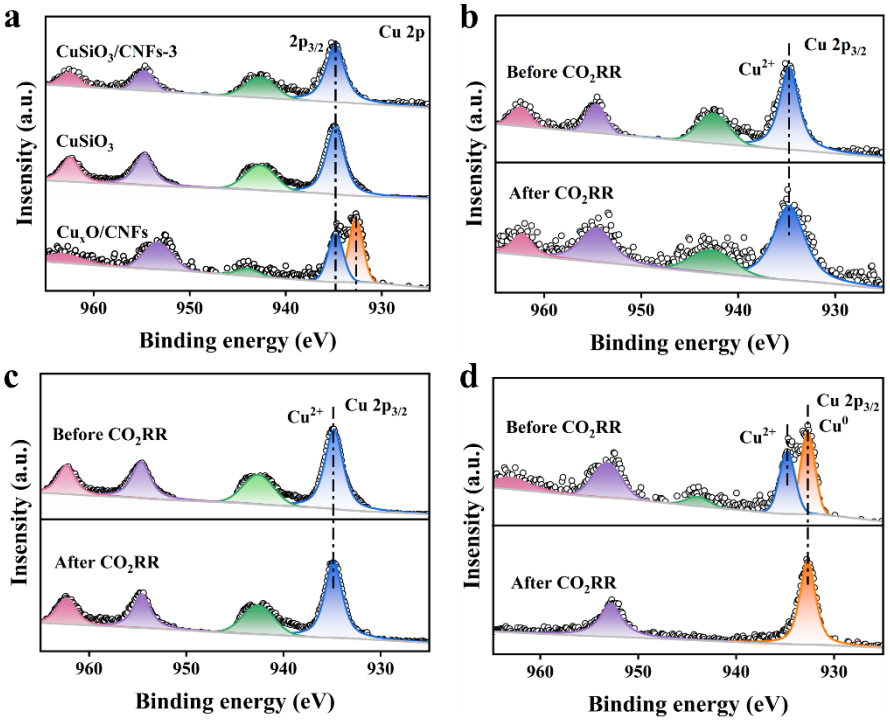

Fig. S25 Cu 2p XPS spectra of $CuSiO_3$/CNFs-3, $CuSiO_3$ and Cu_XO/CNFs sample. (a) before electroreduction and (b-d) after electroreduction.

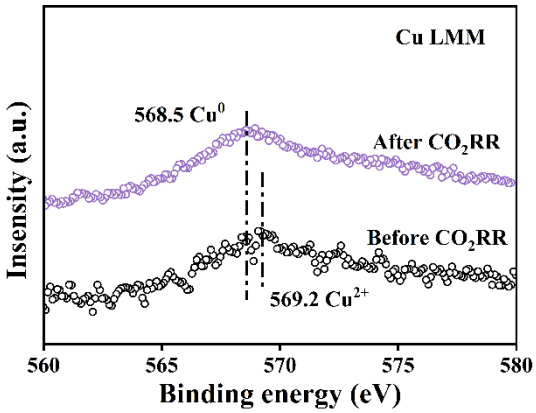

Fig. S26 Cu LMM Auger spectra Cu_XO/CNFs.

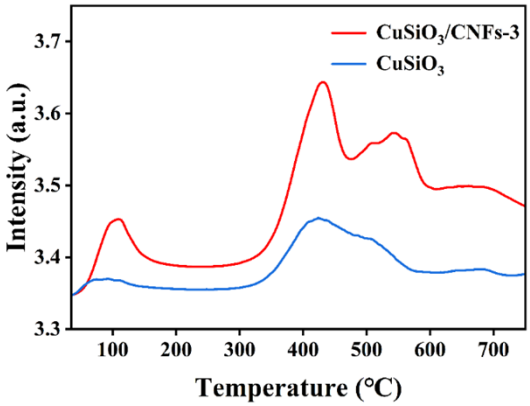

Fig. S27 CO_2−TPD profiles of $CuSiO_3$/CNFs-3.

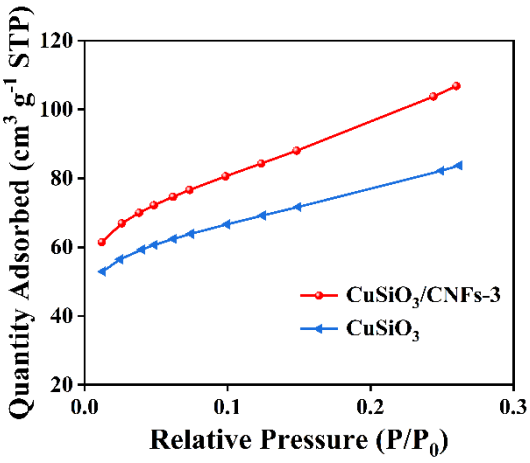

Fig. S28 BET specific surface area test.

Table S1. ICP–OES results of $CuSiO_3$/CNFs-3.

	Cu (At.%)	Si (At.%)
$CuSiO_3$/CNFs-3	46.4%	53.6%

Table S2. Structural parameters extracted from the EXAFS fitting.

Catalysts	path	CN	R/Å	σ^2/Å^2	ΔE(eV)	R-facter
$CuSiO_3$/CNFs-3	Cu-O	3.4	1.93	0.005	3	0.01
	Cu-O-Cu	1.4	2.96	0.008		
	Cu-O-Si	1.0	3.68	0.002		
$CuSiO_3$	Cu-O	3.5	1.95	0.004	3	0.02
	Cu-O-Cu	1.4	2.95	0.008		
	Cu-O-Si	1.1	3.69	0.002		

ΔE^0 was refined as a global fit parameter, returning a value of (3 ± 1) eV. Date ranges: $2.5 \leq k \leq 13$ Å^{-1}, $1.0 \leq R \leq 3.5$ Å. The number of variable parameters is 11, out of total of 15 independent date points, R-factor for this fit is 1%. The distagnces for Cu-O, Cu-O-Cu and Cu-O-Si are form the crystal structure of $CuSiO_3$.

Table S3. The performance comparison of this work with the state-of-the-art results.

Catalysts	Potential (V vs. RHE)	FE_{CH4}(%)	References
$CuSiO_3$/CNFs-3	-1.6	67.8	This work
$CuSiO_X$	-1.27	72.5	[2]
e-Cu_5Si	-1.2	49	[3]
Cu-CeO_X	-1.4	67.8	[4]
Cu_XSi	-1.4	72.9	[5]
CoO/Cu/PTFE	-1.4	60	[6]
Cu_9Ag_1NWs	-1.17	72	[7]
Cu-l	-1.08	57.2	[8]

Table S4. EIS equivalent circuit simulation results.

Sample	R_s	R_{ct}
$CuSiO_3$/CNFs-3	84.74	6.13
Cu_XO/CNFs	84.54	254.7
$CuSiO_3$	86.29	40.82

Reference

[1] Baruch, M. F.; Pander, J. E.; White, J. L.; Bocarsly, A. B. Mechanistic insights into the reduction of CO_2 on tin electrodes using in situ ATR-IR spectroscopy. *ACS Catal.,* 2015, **5**, 2697-3156.

[2] Tan, X.; Sun, K. A.; Zhuang, Z. W.; Hu, B. T.; Zhang, Y.; Liu, Q. G.; He, C.; Xu, Z.Y.; Chen, C.; Xiao, H. et al. Stabilizing copper by a reconstruction-resistant atomic Cu-O-Si interface for electrochemical CO_2 reduction. *J. Am. Chem. Soc.,* 2023, **145**, 8656-8664.

[3] Tao, H. H.; Wang, F.; Zhang, Z. G.; Min,S. X. An in situ exsolved Cu-based electrocatalyst from an intermetallic Cu_5Si compound for efficient CH_4 electrosynthesis. *Nanoscale.,* 2024, **16**, 3430-3437.

[4] Zhou, X. L.; Shan, J. Q.; Chen, L.; Xia, B. Y.; Ling, T.; Duan, J. J.; Jiao, Y.; Zheng, Y.; Qiao, S. Z. Stabilizing Cu^{2+} ions by solid solutions to promote CO_2 electroreduction to methane. *J. Am. Chem. Soc.,* 2023, **144**, 2079-2084.

[5] Zhang, T. Y.; Jin, Y. X.; Lou, S. N.; Yan, T. X.; Xiao, T. T.; Liu, Z. H.; Lin, J. L.; Kuang, S. Y.; Zhang, S.; Ma, X. B. Fine-tuning copper dispersion in Cu/SiO_2 core-shell particles regulates electrochemical CO_2 reduction product selectivity. *Appl. Catal. B: Environ.,* 2024, **353**, 124065.

[6] Li, Y. H.; Xu, A. N.; Lum, Y. W.; Wang, X.; Hung, S. F.; Chen, B.; Wang, Z. Y.; Xu, Y.; Li, F. W.; Abed, J.; et al. Promoting CO_2 methanation via ligand-stabilized

metal oxide clusters as hydrogen-donating motifs. *Nat. Commun.,* 2020, **11**, 6190.

[7] Choi, C. S.; Cai, J.; Lee, C. S.; Huang, Y.; Lee, H. K.; Xu, M. J. Intimate atomic Cu-Ag interfaces for high CO_2RR selectivity towards CH_4 at low over potential. *Nano Res.,* 2021, **14**, 3497-3501.

[8] Zhang, Y.; Zhou, Q.; Qiu, Z. F.; Zhang, X. Y.; Chen, J. Q.; Zhao, Y.; Gong, F.; Sun, W. Y. Tailoring coordination microenvironment of Cu(I) in metal-organic frameworks for enhancing electro-reduction of CO_2 to CH_4. *Adv. Func. Mater.,* 2022, **32**, 2203677.